Microstructural and mechanical properties of a novel cobalt and titanium free maraging steel for laser powder bed fusion

Giorgia Lupi [a], Eleonora Bettini [b], Faraz Deirmina [b,**], Riccardo Casati [a,*]

[a] Politecnico di Milano, Department of Mechanical Engineering, Via G. La Masa 34, 20156, Milano, (MI), Italy
[b] Powder R&D, Sandvik Additive Manufacturing, Sandviken, Sweden

ARTICLE INFO

ABSTRACT

Maraging steels are widely used in Additive Manufacturing due to their good processability and outstanding combination of strength and toughness. 18Ni300 is one of the most employed maraging steels. However, it contains cobalt, which has recently been strictly regulated due to its environmental and health hazards, having been classified as carcinogenic. Moreover, this steel contains Ti, showing a high affinity for oxygen, leading to high oxide fractions in powder and final parts. In the current work an ultrahigh strength Co and Ti free maraging steel for AM was processed and characterized. The results were then compared to 18Ni300. The novel alloy, processed with Powder Bed Fusion - Laser Beam (PBF-LB) shows hardness, yield strength, and tensile strength of 525 HV1, 1475 MPa, and 1588 MPa, respectively, after solution annealing and aging treatments.

1. Introduction

Maraging steels are age-hardening high-strength steels with very low carbon content. The high strength levels can be achieved by optimizing the chemical composition, and selection of the right sequence of heat treatments, reducing phenomena such as the reversion of martensite into austenite, the coarsening of the microstructure, and the precipitation of unwanted phases [1]. The presence of substitutional alloying elements such as Mo, Ti, and Al causes age-hardening in Fe–Ni martensite by precipitation of nano-sized intermetallic particles (e.g., Ni_3Ti, Ni_3Mo, NiAl, Fe_7Mo_6, and Laves phase) [2–4].

Due to their good combination of mechanical properties and weldability, maraging steels are widely commercialized in laser based Additive Manufacturing (AM) processes, such as Powder Bed Fusion – Laser Beam (PBF-LB) technology [5,6]. Crack free and fully dense parts with complex geometries and enhanced mechanical properties can be readily produced. Their applications vary from mold and die making industry to high-performance parts, e.g., in the aerospace industry [7–10].

In AM, the most widely used maraging steel is 18Ni300 where the main alloying elements are nickel, cobalt, molybdenum, and titanium. This alloy shows excellent strength and toughness, with the main strengthening mechanisms being precipitation hardening of Fe–Ni martensite, and solid solution hardening [11–14]. In this alloy system,

Co lowers the solubility of Mo and Ti, leading to enhanced precipitation kinetics of intermetallic phases such as nano-sized Ni_3Ti, and Ni_3Mo. Co, up to ~10 wt%, also raises the martensite start (Ms) temperature, enabling the addition of higher amounts of substitutional alloying elements without leading to the formation of residual austenite [15,16]. However, cobalt remains a challenging element in 18Ni300 maraging steel, because of its high cost and more importantly its toxicity, leading to serious environmental and social issue [17,18].

In recent years, several efforts have been made to develop novel cobalt-free maraging steels [19–23]. In cobalt free maraging steels, titanium and aluminum concentrations are increased since they are responsible for the formation of strengthening precipitates during aging treatments [24]. However, increasing the amount of titanium can lead to the formation of grain boundary titanium carbonitrides, causing anisotropy of the plasticity and reducing ductility. The increase in aluminum concentration is responsible for limited hardening of martensite and lowers ductility both before and after aging [16,19]. Ti and Al are also very prone to form oxides during gas atomization translating into inclusions in the printed material. Because of these reasons, the processing of such powders is mostly realized by expensive atomization routes such as Vacuum Inert Gas Atomization (VIGA) to ensure minimal loss of Ti, and Al during the atomization, avoiding nitrogen pick-up which eventually forms TiN inclusions, and achieving

Table 1
Chemical composition of the feedstock powder.

Chemical composition (wt%)									
	C	Ni	Co	Mo	Ti	Al	Si	Mn	Fe
Co–Ti free nominal	<0.08	11.00–13.00	<0.10	7.00–8.00	<0.10	<0.10	<0.30	<0.30	Bal.
Co–Ti free powder	0.04	13.00	–	7.50	0.01	0.05	0.10	0.10	Bal.
18Ni300 Nominal	<0.03	18.00	9.00	4.80	0.70	<0.10	<0.10	<0.10	Bal.
18Ni300 Powder	0.02	18.00	10.10	4.75	0.70	0.06	0.05	0.05	Bal.

very low oxygen contents in the final product. Therefore, developing Co, and Ti free maraging steel powders enabling the use of the more cost-efficient routes such as Inert Gas Atomization (IGA) is of both technological and industrial interest.

In the current work, an ultrahigh strength Co, and Ti free maraging steel developed by Sandvik Osprey (Neath, UK) using inert gas atomization was fabricated by PBF-LB. The microstructure, hardness, and mechanical properties were studied before and after ageing heat treatments. Based on the thermal analysis results, and mechanical properties, an optimized ageing scenario was proposed. The results were then compared to commercial 18Ni300, fabricated and tested using the same testing conditions.

2. Materials and methods

2.1. Powder chemical composition

The starting powders chemical compositions are listed in Table 1. The Co, and Ti free (herein after Co–Ti free) contains lower Ni than that of 18Ni300, to guarantee a reasonably high martensite start temperature (Ms) in the absence of Co [25]. The absence of Co and lower Ni, leading to increased solubility of Mo in the martensitic matrix and more sluggish precipitation of Ni$_3$Mo, is partially compensated by increased Mo content to ensure sufficient age hardening effect [25]. Al levels are kept below 0.10 wt% and are only used as a deoxidizing agent in the melt. Concerning the particle size distribution, both feedstock powders had a D10 of to 15 μm and a D90 of 53 μm. The particles size distribution measurements were performed by laser diffraction analysis according to ISO 13320.

2.2. Thermo-Calc simulations

The Thermo-Calc software [26] with the TCFE12 database was used to calculate the equilibrium step diagrams for the two alloys. In the calculations a molar amount of 1, and a pressure of 10^6 Pa, was selected. Scheil-Gulliver simulations were performed to understand the far from equilibrium rapid solidification behavior of the alloys. The start temperature was set to 2000 °C, and the temperature step of 1 K was used. Scheil calculations were run using the solute trapping option (TCFE12-MOBFE6) developed for the laser-based AM processes, by setting a laser scan speed of 950 mm/s and the angle between solid/liquid interface and scanning direction (α) was set as default value in the software (i.e., 45 deg) as the primary purpose of the calculations in this paper was to have a semi-quantitative comparison of the rapid solidification behavior of the two alloys [27]. Solute trapping model is based under the assumption that only the primary solid phase is the dendrite forming phase, in which, solute trapping is induced by rapid solidification. Therefore, the amount of other solid phases is affected by the solute trapping and solidification speed. Additionally, the martensite fractions vs. temperature, were calculated using the property module in Thermo-Calc software. In all conditions, based on the equilibrium step diagram results, a solution annealing temperature of 1000 °C, with a prior austenite grain size of 50 μm, was selected for the calculation of martensite fractions upon cooling.

Table 2
Optimized printing parameters.

Laser Power (W)	Scanning speed (mm/s)	Hatch spacing (mm)	Layer thickness (μm)	VED (J/mm^3)
285	950	0.110	40	68.2

Table 3
Hardness (HV1) results for the alloys in as built and solution annealed state.

	As built	Solution annealed
Co–Ti free	368 ± 9	347 ± 8
18Ni300	365 ± 5	348 ± 4

2.3. Processing

Test cubes (15 × 15 × 15 mm^3) and samples for mechanical characterizations were fabricated using an EOS M290 LPBF machine equipped with 400 W Yb-fiber laser. For the process optimization trials, the volumetric laser energy density (VED) was considered (Eq. (1)).

$$VED\left(\frac{J}{mm^3}\right) = \frac{P}{v.h.t} \tag{1}$$

where P (W) is the laser power, v (mm/s) being laser scanning speed, h is the hatch spacing in mm, and t is the layer thickness in mm.

Hatch spacing (0.110 mm) and layer thickness (0.040 mm) were kept unchanged, while twelve different combinations of laser power (from 245 W to 365 W), and laser speed (750 mm/s to 1117 mm/s) resulting in a VED range of ~62–~86 J/mm^3 were examined to achieve parts with >99.9 % relative density. Relative density was measured using light optical microscope (LOM) micrographs on ground (up to 1200 grit) and polished (3, and 1 μm cloth) metallographic cross-sections. The optimized parameters reported in Table 2 were used to print the two alloys (see Table 3).

The samples were then solution annealed (1000 °C, 2 h) in a furnace with a controlled Ar atmosphere, followed by air cooling. Then samples were aged for different times at 460 °C, 490 °C, 525 °C, and 600 °C, to construct the aging curves (hardness vs. time). All machining operations to obtain specimens for mechanical testing were carried out after the age-hardening heat treatment.

2.4. Mechanical testing

Vickers microhardness tests (kg$_f$/mm^2) were performed using a Future-Tech FM-810 system. The samples were subjected to a load of 1 kg for dwell time of 10 s (i.e., HV1). Vickers hardness measurements were carried out on carefully ground and polished metallographic cross-sections according to the ASTM E92-82 standard [28]. Six measurements were performed for each condition.

Tensile tests were performed using an MTS-Alliance RT/100 universal testing machine. The specimens have a gauge length of 24 mm and a diameter of 4 mm. Three tensile specimens for each of the selected conditions were tested at room temperature.

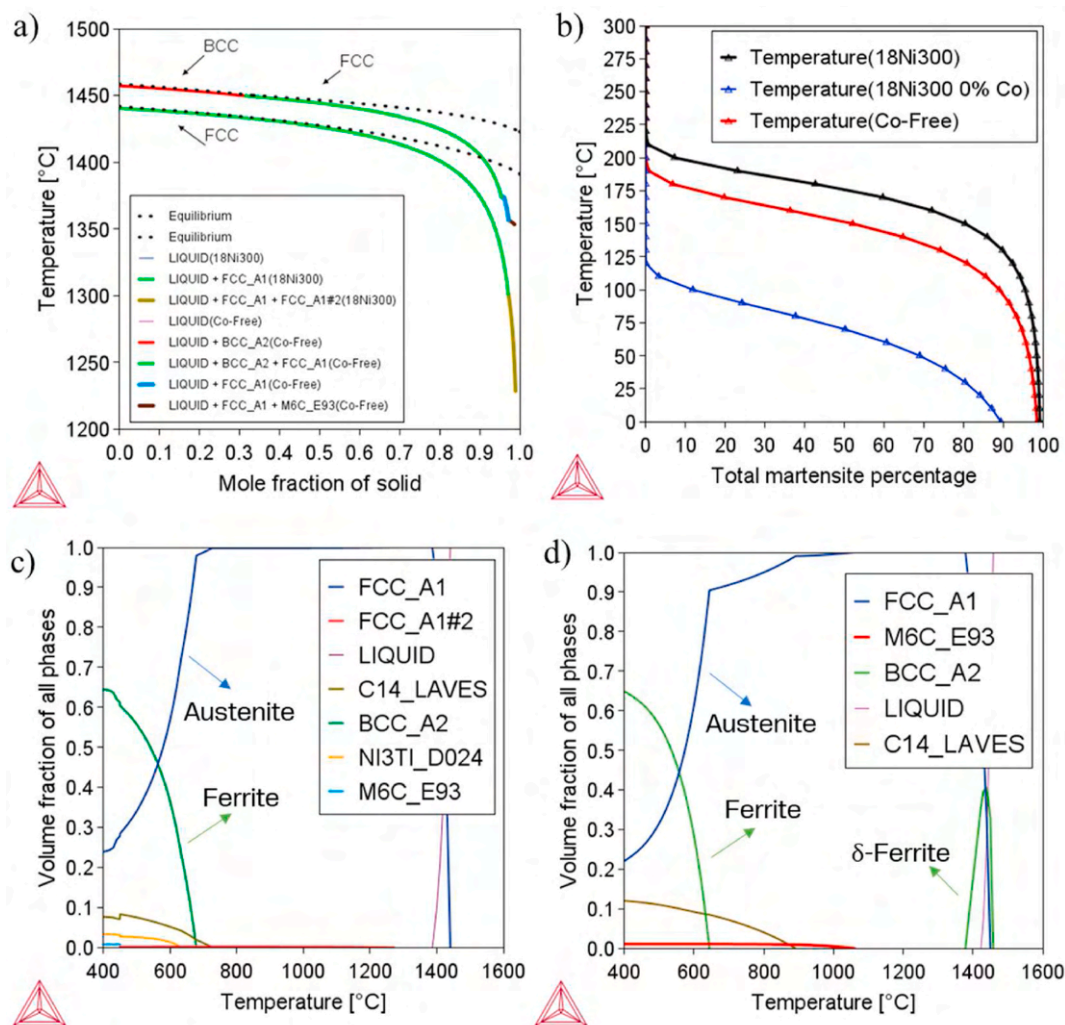Charpy V notch (CVN) impact toughness tests were performed

Fig. 1. a) Scheil solidification curves, b) Total martensite percentage versus temperature, equilibrium step diagrams of c) 18Ni300, note FCC_A1#2 is TiC, and d) Co–Ti free alloy.

according to ASTM E23-23a [29]. The size of the standard specimen is $10 \times 10 \times 55$ mm. Three specimens for each of the selected conditions were tested at room temperature.

2.5. Material characterization

Diffraction patterns were collected using a Rigaku SmartLab X-Ray diffractometer (XRD) employing Cu Kα radiation. The data were obtained in the diffraction angle range of $40° \leq 2\theta \leq 80°$, with a step width of $0.01°$ and a velocity of $1°$/min. Differential scanning colorimetry (DSC) tests were performed using a Labsys Setaram calorimeter. Heating ramps ($10 °C$/min) programmed to isochronally heat the samples up to $1200 °C$.

The analysis of microstructure was performed by LOM, and a Field Emission Scanning Electron Microscope (FE-SEM) (Zeiss Sigma 500), equipped with energy dispersive X-ray analysis (EDX). Samples for metallography were prepared following common grinding and polishing procedures, Chemical etching was performed by Nital 2% or Kalling's reagent to reveal the microstructural features. Electron back scatter diffraction (EBSD) analysis was conducted using a Symmetry EBSD detector on FE-SEM on ground and polished cross-sections. A 20 kV accelerating voltage with a working distance of 15 mm was used for the EBSD analysis.

3. Results and discussion

3.1. Thermodynamic simulations

Scheil solidification curves are reported in Fig. 1a. In 18Ni300, the solidification starts with the formation of austenite (FCC_A1) and with the increase in mass fraction of the solid, the remaining liquid to solidify progressively enriches in alloying elements. The solidification ends with the formation of TiC (FCC_A1#2). It is interesting to note that for the Co–Ti free alloy, the primary phase is the ferrite (BCC_A2) followed by austenite (FCC_A1) as the volume fraction of the solid increases, and finally Mo rich carbides (M_6C) are formed. Another noticeable difference is the very small Scheil solidification temperature range for the Co–Ti free alloy as a result of its leaner composition. Applying the thermodynamic based martensite start (Ms) modeling by Thermo-Calc, the Ms in 18Ni300 and the Co–Ti free alloy, using the nominal chemical compositions, were ~215 °C and ~200 °C, respectively. In both case at about room temperature, over 95% of the austenite transforms to martensite (Fig. 1b). The need to reduce Ni in the absence of Co to keep the martensitic transformation temperatures sufficiently high is also illustrated by comparing the temperatures of 18Ni300 composition without Co. The equilibrium step diagrams also point out the stability of delta ferrite at high temperature for the Co–Ti free material compared with that of 18Ni300 showing no delta ferrite at high temperature (Fig. 1c and d). Ferrite and austenite stability, and equilibrium volume
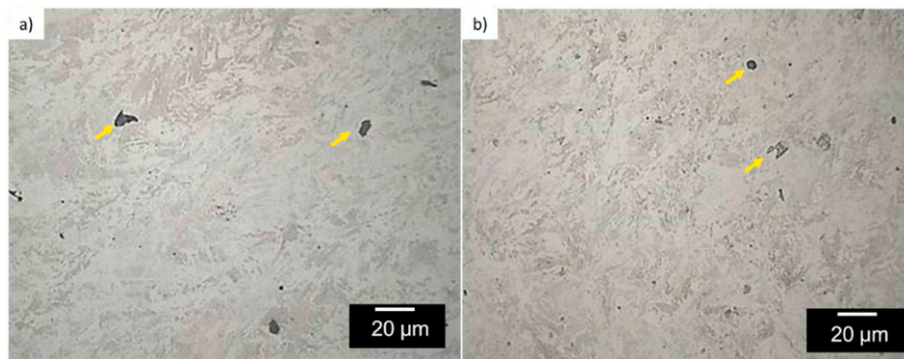
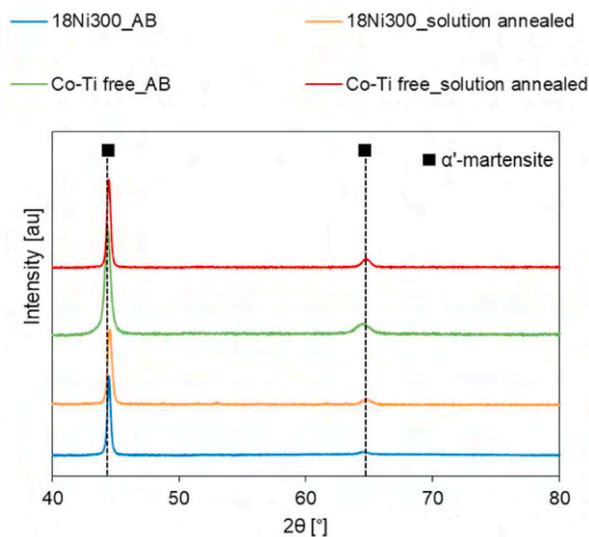**Fig. 2.** LOM images of a) 18Ni300 and b) Co–Ti free in as built state.

Fig. 3. XRD patterns of as built and solution annealed condition of 18Ni300 and Co–Ti free alloy.

characterized as oxide phases containing mainly Si and Al. Due to the lower amount of Al and Ti in the novel alloy, it is reasonable that this steel possesses an enhanced cleanliness. The presence of these oxide inclusions was also detected in other additively manufactured maraging steels [13,24,31]. Inclusions average area fraction normalized by the total area are 0.4% and 0.12% for 18Ni300 and Co–Ti free alloy in as-built condition, respectively. These measurements were performed on three representative micrographs for each alloy.

Fig. 3 summarizes the XRD diffractograms acquired from samples in as built and solution annealed conditions. No differences were detected between the two different compositions of the alloy or between the as built and solution annealed conditions. Indeed, only two peaks associated with martensite (α) can be observed. No peaks associated to residual austenite (γ) were found, meaning that fraction of residual austenite is below the XRD detection limit (i.e., < 2–3 vol% using Cu K-alpha radiation source for steels [32]) in all the samples, in agreement with martensite fractions simulations in Fig. 1b. The as built microstructure comprises a martensitic matrix and a cellular solidification structure characterized by intercellular micro-segregation appearing brighter in back scatter electron (BSE) micrographs (Fig. 4a). The cell size is around 1 μm, while the intercellular micro-segregation has an average thickness of 120 ± 17 nm. According to the high magnification EBSD maps, 2.6 ± 0.8 vol% retained austenite was found at the intercellular micro-segregation in as built material (Fig. 4b, and the inset). It is very well elaborated and widely reported that the cellular structure in rapidly solidified PBF-LB processed alloys is a result of the constitutional undercooling accompanied by the micro-segregation of alloying elements at the intercellular/inter-dendritic regions, thus leading to a local drop in martensite start temperature [33,34]. This is also shown in supplementary file 1 using Scheil modeling coupled with diffusion calculator in Thermo-calc software where martensite start temperature drops to below 100 °C at the micro-segregated areas resulting in chemical stabilization of RA. This phenomenon is due to the gradual enrichment of alloying elements, especially Ni, Mo and C from the cell core to the cellular boundaries. In solution annealed condition, where the microstructure is homogenized and micro-segregation is removed by diffusion of alloying elements at high temperature (Fig. 4c), the microstructure is fully martensitic, and RA becomes barely detectable even by EBSD analysis (Fig. 4d). A full description of the microstructural features in 18Ni300 can be found in the previous work of the authors [13].

The very low vol% of RA provides a suitable condition for direct aging of the martensitic as built microstructure without the need for prior solution annealing. Moreover, an obvious peak broadening is evident for the AB Co–Ti free samples compared to that of solution annealed. This represents larger lattice defects density (e.g., dislocations) in the rapidly cooled laser melted as built material [35]. This difference seems to be less pronounced in 18Ni300 samples. This needs further investigation which is outside the scope of the present work.

fractions at lower temperatures are similar for both alloys. Within the ageing temperature interval (e.g., 400–600 °C), two main intermetallic phases are present in 18Ni300, namely Ni$_3$Ti, and Laves. It is well known that, even if laves (Fe$_2$Mo) is an equilibrium phase at those temperatures, given a sufficient cooling rate from the solution annealing temperature, ageing of the quenched or air-cooled martensite results in the precipitation of nano sized metastable Ni$_3$Mo instead of that of equilibrium laves. Longer times or high temperatures are needed for the Ni$_3$Mo to transform to the equilibrium laves phase [30]. In the Co free alloy, the only major strengthening phase is Ni$_3$Mo (or laves as shown in equilibrium diagram), as a result of the absence of Ti. Due to the increased wt.% of Mo in Co–Ti free alloy, the stability of laves phase is extended to slightly below 900 °C. The laves stability temperatures in 18Ni300 is ~725 °C according to the equilibrium diagram.

3.2. Material characterization and mechanical testing
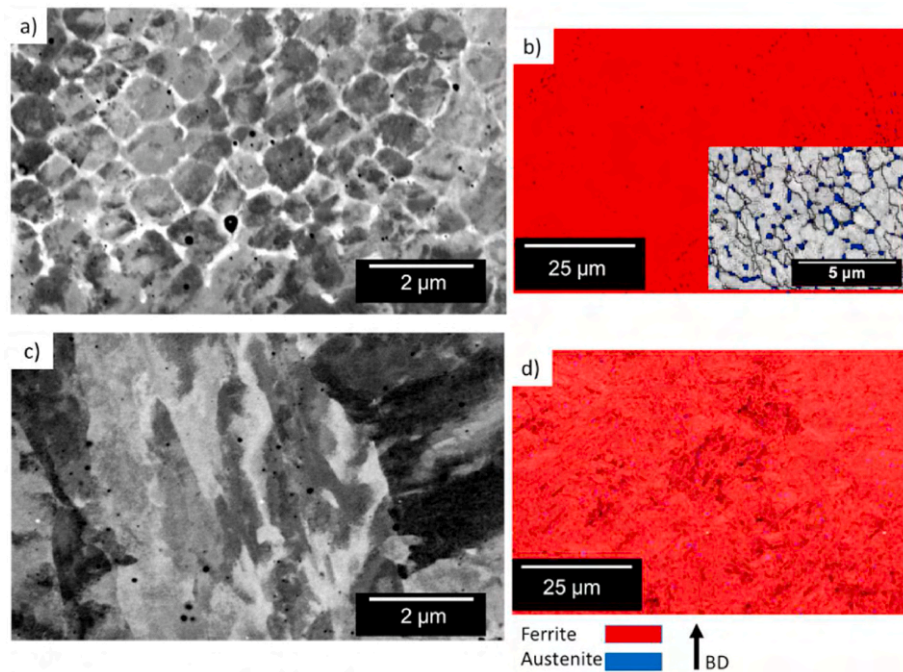
3.2.1. Microstructure and phases prior to ageing

Fig. 2a and b shows LOM images of the 18Ni300 and Co–Ti free steel in the as built condition, respectively. The 18Ni300 and Co–Ti free alloy present similar microstructural features (i.e., martensitic microstructure). The presence of non-metallic inclusions in both microstructures are evident. In case of 18Ni300 the inclusions seem to be larger with higher vol% compared with the novel alloy. According to EDS analysis, these inclusions were preferentially Al- and Ti-rich oxides in 18Ni300. Non-metallic inclusions found in matrix of the Co–Ti free alloy were

Fig. 4. a) SEM-BSE micrograph of as built condition featuring a cellular solidification structure, b) EBSD phase map in as built state, inset showing RA stabilization at the intercellular micro-segregation (in blue), c) SEM-BSE micrograph in solution annealed condition, and d) EBSD phase map in solution annealed state. (For interpretation of the references to color in this figure legend, the reader is referred to the Web version of this article.)
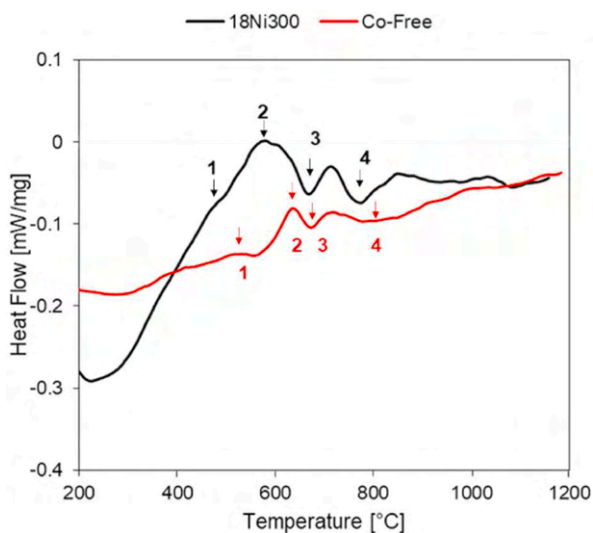
Fig. 5. DSC curves of 18Ni300 and Co–Ti free alloy.

3.2.2. DSC analysis, ageing kinetics

DSC analyses were used to conduct a comparison study of the aging behavior of the two alloys. DSC scans at a heating rate of 20 °C/min are reported in Fig. 5. Four characteristic peaks for 18Ni300 and Co–Ti free alloy can be identified. In both cases, the first exothermic peak (peak #1) represents the formation of Mo rich M_2C carbides or coherent precipitation zones [36–38]. The second exothermic peak (peak #2) represents the formation of the main strengthening precipitates ($Ni_3(Mo, Ti)$) phases followed by equilibrium Fe_2Mo (laves) and Fe_7Mo_6 (µ phase) in case of long holdings at ageing temperature [37,39,40]. The endothermic peaks (peaks #3 and #4) respectively refer to austenite reversion by diffusion (i.e., local Ni enrichment due to precipitate dissolution or transformation of Ni_3Mo to equilibrium Fe_2Mo, or Fe_7Mo_6) and austenite transformation by shear, respectively [34,41,42].

It is reported that the more intense 2nd exothermic peak in 18Ni300 is related to the precipitation of metastable Ni_3Mo and Ni_3Ti in peak aged condition [37,40]. In the absence of Ti, the second exothermic peak in Co–Ti free alloy must be only related to the Mo rich precipitates (e.g., metastable Ni_3Mo). This peak is not only characterized by a lower intensity compared with that of 18Ni300, but also is shifted towards higher temperatures, suggesting that the precipitation kinetics are different. Even if in the Co–Ti free alloy, the Mo content is almost twice that of 18Ni300, the precipitation kinetics in 18Ni300 is faster. It is suggested that Co lowers the solid solubility of Mo in Fe–Ni martensite. This leads to enhanced precipitation kinetics, more uniform and larger vol% of Mo containing intermetallic precipitates in Co containing maraging steels. Following the pioneering work of Sha [43], it was quantitatively shown that in aged cobalt free and cobalt containing 18Ni–5Mo-0.7Ti maraging system, the same families of Ti rich and Mo rich precipitates exist. However, the Mo rich phase only forms at a later stage of aging in the Co-free steel (i.e., longer times or higher ageing temperatures) and is characterized by lower vol% compared with that of Co containing system. In addition to this, Mo level in Ni_3Ti precipitates is much lower in Co-free steel compared with Co-bearing counterpart. These quantitative evaluations clarified that a major role of cobalt in maraging steels is to lower the solubility of Mo in martensite, leading to an increased precipitation kinetics as well as volume percentage of Mo containing precipitates thus increasing the strength. The latter will be discussed shortly in section 3.2.3 where the ageing curves are shown.

Lastly, the delay in austenite reversion in Co–Ti free alloy is ascribed to its lower Ni content. This accounts for its enhanced softening resistance at elevated temperatures, which is promising in view of its application in tooling.

3.2.3. Hardness and aging curves

Hardness of the Co–Ti free alloy and 18Ni300 were measured both for as built and solution annealed conditions. The two alloys do not show significant differences in hardness values. In as built state, both alloys show a hardness of ~370 HV1, while the hardness is decreased to ~350 HV1 after solution annealing. It is well known that increased dislocation
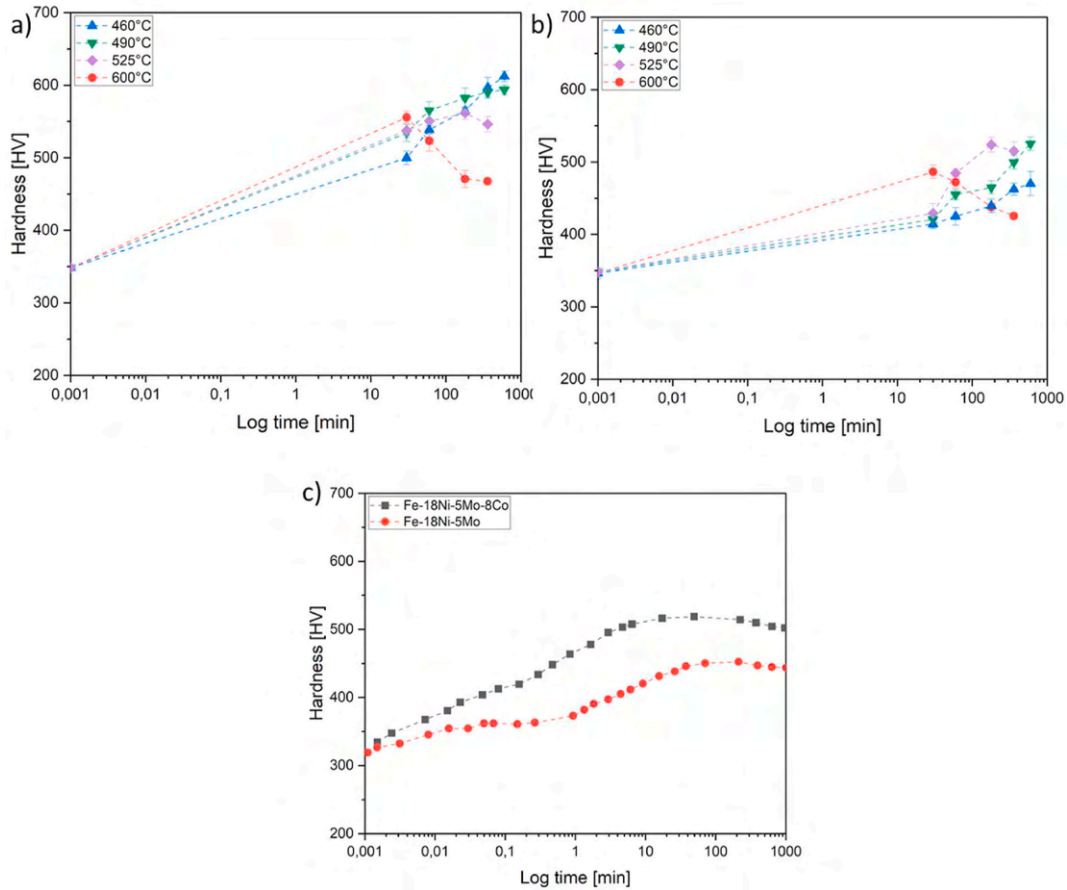
Fig. 6. Vickers hardness vs. aging time of a) 18Ni300, b) Co–Ti free samples collected at different aging temperatures, c) Fe–18Ni–5Mo–8Co and Fe–18Ni–5Mo (aging temperature 480 °C) reconstructed from Ref. [46].

density in rapidly solidified AM components is responsible for higher hardness (strength) in as built condition [44,45].

Aging curves for both materials are reported in Fig. 6. In 18Ni300

alloy (Fig. 6a), by ageing at 460 °C, a progressive increase in hardness is witnessed, it appears that hardness does not show a drop within the maximum ageing time, suggesting that at this temperature the kinetics

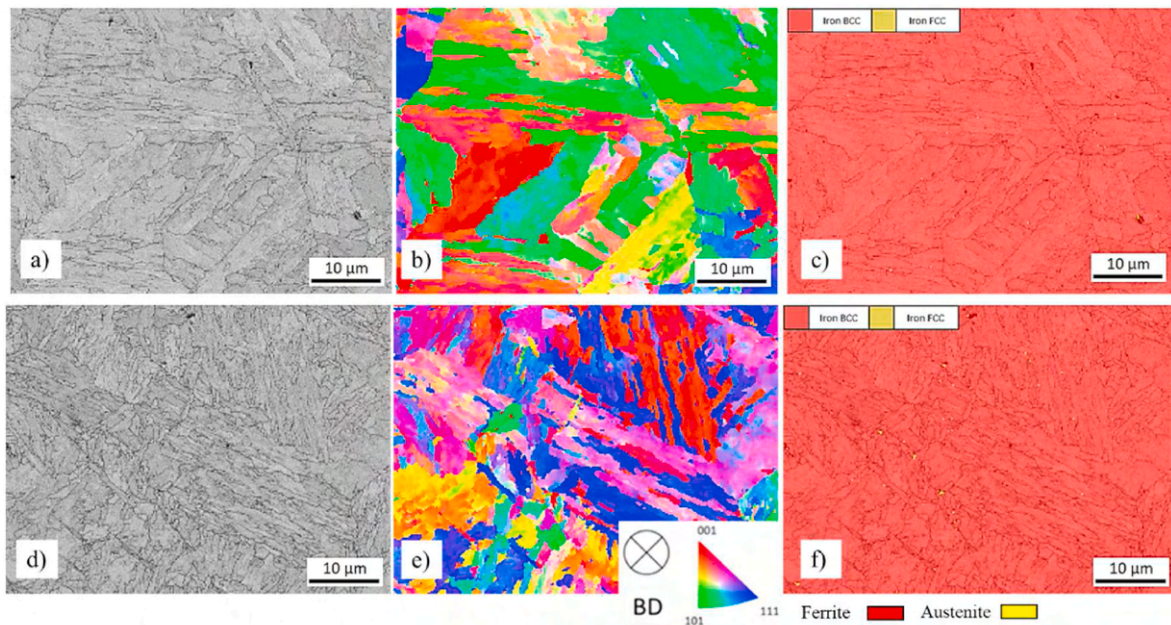**Fig. 7.** EBSD result for 18Ni300: a) BC image, b) IPFz map in solution annealed and aged condition (490 °C, 6 h), c) phase map, and Co–Ti free alloy: d) BC image, e) IPFz map, and f) phase map in solution annealed and aged condition (525 °C, 3 h).
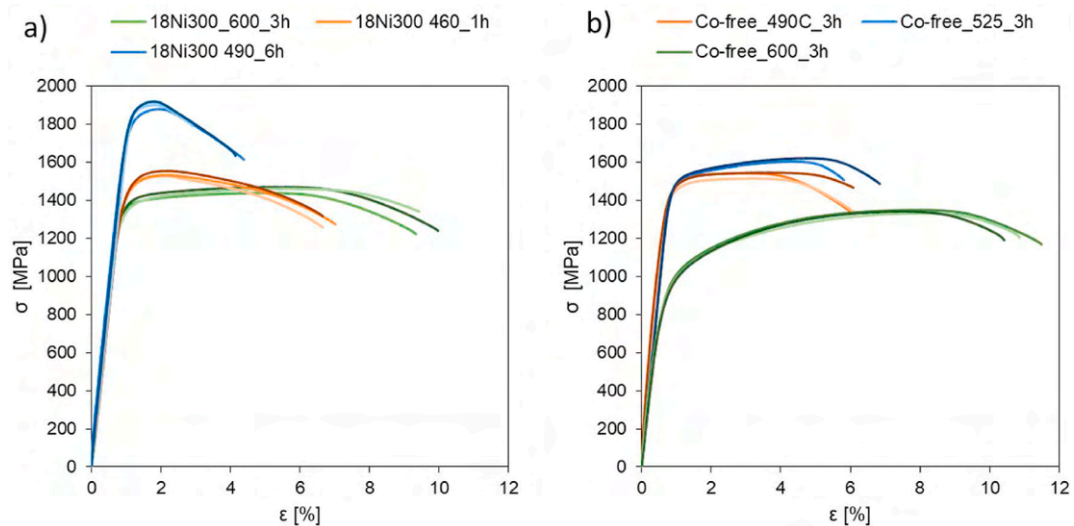
Fig. 8. Stress vs. strain records of a) 18Ni300 and b) Co–Ti free samples collected at different aging temperatures.

Table 4
Tensile properties as a function of aging temper.

18Ni300			
Aging condition	460 °C/1 h	490 °C/6 h	600 °C/3 h
YS (MPa)	1404 ± 35	1844 ± 24	1305 ± 6
UTS (MPa)	1539 ± 11	1900 ± 16	1456 ± 13
ε (%)	6.8 ± 0.1	3.8 ± 0.6	9.7 ± 0.3
Co–Ti Free			
Aging condition	490 °C/3 h	525 °C/3 h	600 °C/3 h
YS (MPa)	1435 ± 11	1475 ± 9	880 ± 22
UTS (MPa)	1534 ± 14	1588 ± 19	1342 ± 7
ε (%)	6.4 ± 0.4	6.4 ± 0.6	10.8 ± 0.3

of precipitate coarsening or austenite reversion is still low. The maximum hardness of ~600 HV1 was achieved at the longest time designated in this study (i.e., 10 h). At 490 °C, a peak hardness of 590 HV1 was achieved by 3 h holding, after this point, the hardness was almost steady although with a negligible evident drop. At the highest temperature levels (525 °C and 600 °C) the peak ageing was achieved at shorter times (i.e., 1 h and 0.5 h, respectively). At these temperatures, hardness dropped more rapidly by prolonging the ageing due to over-aging, and enhanced diffusion-controlled austenite reversion. For the Co–Ti free alloy (Fig. 6b), at the same ageing temperatures, the ageing time to reach peaks-hardness was delayed compared with 18Ni300 in agreement with lower precipitation kinetics observed by DSC analysis. For instance, at 490 °C, the hardness keeps its increasing trend even after 10 h of ageing, and at 525 °C a peak age hardness of 525 HV was achieved after 3 h (i.e., 2 h longer than that of 18Ni300). These results agree with the work of Magnee et al. [46] whereby removing Co from 18Ni300 chemistry led to a more sluggish precipitation kinetics, as well as lower peak-aged hardness compared with the Co containing counterpart (Fig. 6c). At higher ageing temperature of 600 °C, the aging kinetics seem to become similar for both alloys due to the enhanced diffusional reactions. The highest hardness value (525 HV), considering the ageing conditions in this study, was achieved after 3 h aging at 525 °C.

Based on the hardness test results, further analyses on mechanical behavior were focused on samples aged at 490 °C for 3 h (underaged), 525 °C, 3 h (peak aged), and 600 °C, 3 h (over-aged) for the Co–Ti free alloy. For the 18Ni300 maraging steel, the selected temperatures and times were 460 °C for 1 h and 490 °C for 6 h, and 600 °C, 3 h respectively.
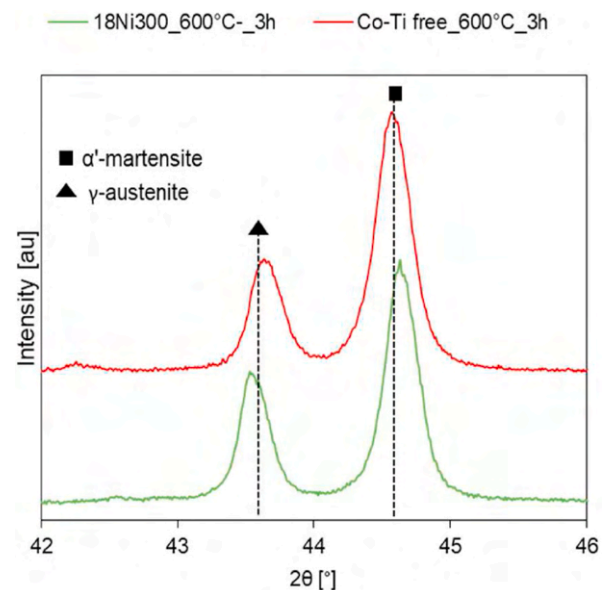

Fig. 9. XRD patterns of 18Ni300 and Co–Ti free alloy in over-aged condition.

### 3.2.4. Microstructural characterization after age hardening

According to EBSD band contrast (BC), and inverse pole figure (IPF) maps, in solution annealed and aged specimens, the microstructure is characterized by a lath martensite structure where lath martensite shows the martensite packet and block hierarchy in both alloys (Fig. 7 a, b, and d, e). The microstructures are comparable to the microstructure of conventionally fabricated maraging steel [10].

The phase maps overlaid on BC images show that the volume fraction of austenite (retained and reverted austenite) is extremely low (i.e., <0.08%) for both alloys, confirming that the ageing scenario to achieve peak hardness excludes excessive austenite reversion responsible for softening of the material (Fig. 7c and f).

3.2.5. Tensile tests

Tensile tests at room temperature were performed on samples aged at different times and temperatures. Tensile curves for both materials are reported in Fig. 8. Table 4 summarizes the main average data collected.

The results are in good agreement with the results of the hardness
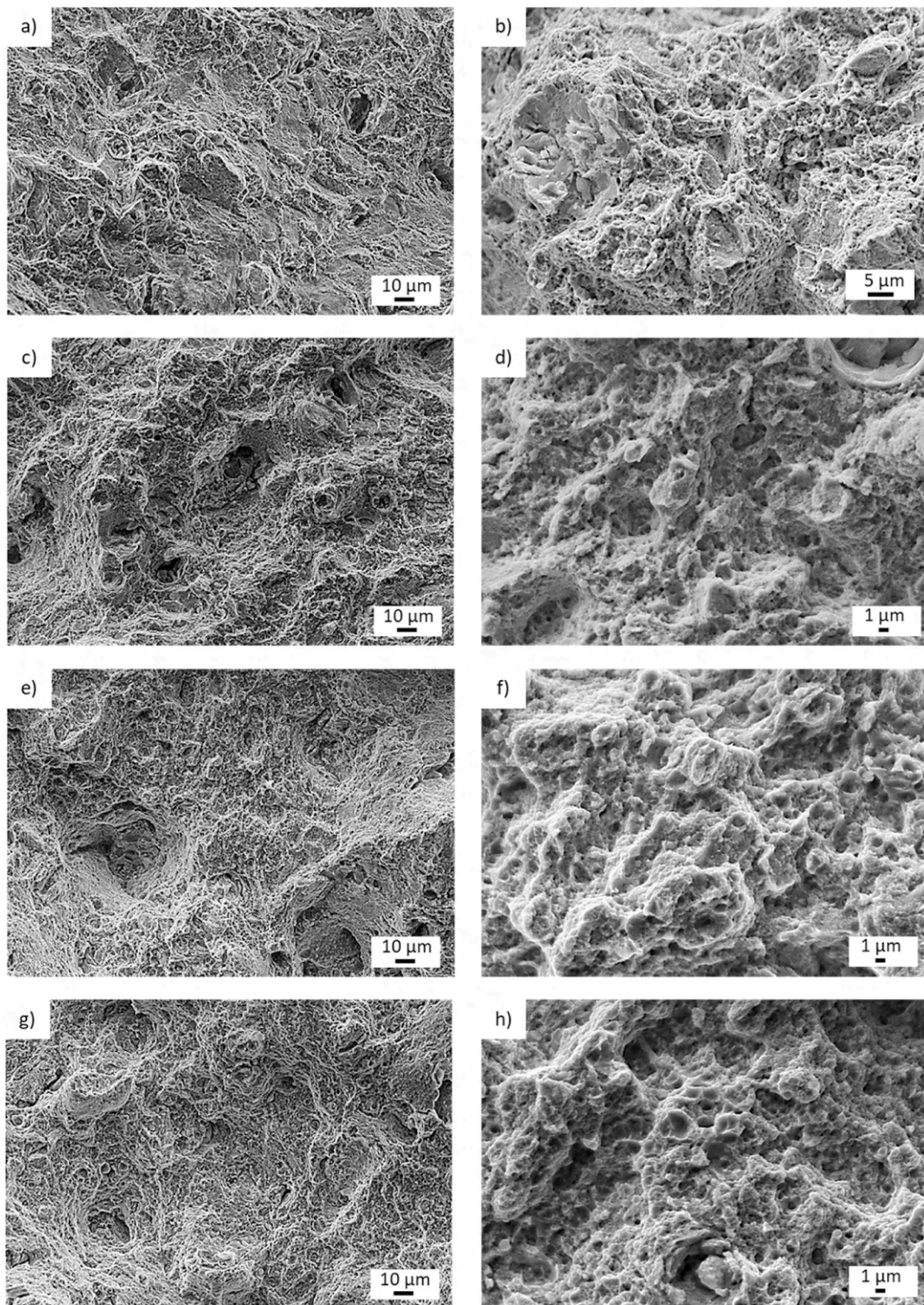
Fig. 10. SEM micrographs of the fracture surfaces of 18Ni300 in a,b) peak-aged and c,b) over-aged conditions and Co–Ti free alloy in e,f) peak-aged and g,h) over-aged conditions.

tests (see Fig. 6). Both alloys showed the highest YS and UTS at their peaks-strength (490 °C/6 h for 18Ni300 and 525 °C/3 h for Co-free steel). The highest YS and UTS values of the Co–Ti free alloy are lower than those of the 18Ni300; however, the elongation at fracture is higher (i.e., 6.8% vs. 3.8%).

In underaged condition, 18Ni300 showed a yield strength of 1400 MPa comparable to that of Co–Ti free material in underaged state (i.e., 490C, 3 h). The UTS and elongations were essentially similar.

In the over-aging condition (600 °C/3 h), UTS (1456 MPa, and 1342 MPa for 18Ni300, and Co–Ti free alloy, respectively) and YS drastically decreased for both compositions, accompanied by a significant increase in ductility (ε (%) ~11). This phenomenon can be related to the formation of reverted austenite, and precipitate coarsening leading to a drastic decrease of Orowan strengthening contribution [47,48]. XRD patterns in Fig. 9 show the presence of the γ-austenite peaks. This confirms that at aging temperatures higher than 600 °C, reversion of

Table 5
Energy absorbed as a function of aging temper.

18Ni300			
Aging condition	460 °C/1 h	490 °C/6 h	600 °C/3 h
Energy absorbed (J)	11.0 ± 0.8	8.3 ± 1.2	10.5 ± 0.5
Co–Ti Free			
Aging condition	490 °C/3 h	525 °C/3 h	600 °C/3 h
Energy Absorbed (J)	6.0 ± 0.0	5.3 ± 0.5	10.5 ± 0.5

martensite into austenite occurs, leading to a decrease in hardness and strength of the material [49]. Moreover, the amount of reverted austenite seems to be lower in Co–Ti free alloy compared with that of 18Ni300, another confirmation on the DSC results (Fig. 5) manifesting the more sluggish reversion kinetics in this alloy due to the lower Ni content.

The fracture surfaces of the two alloys in peak-aged and over-aged conditions are shown in Fig. 10. The analysis reveals the presence of dimples in the case of 18Ni300 steel in the over-aged condition and Co–Ti free alloy in both conditions. Dimples indicate micro-void coalescence and deformation by slip and are typical features of ductile failure. Dissimilarly, the fracture surface of the 18Ni300 in peak-aged condition shows the presence of cleavage facets that alternates to areas characterized by dimples. The generally higher elongation of Co–Ti free alloy is mostly attributed to its lower strength, and additionally can be a consequence of the enhanced cleanliness compared with 18Ni300.

3.2.6. Charpy impact tests

Charpy impact tests were performed to evaluate the effects of the aging and solution annealing on the toughness; the results are reported in Table 5. For both alloys, the aging conditions that led to peak-hardness were associated with the lowest energy absorbed. A significant decrease in impact toughness with aging heat treatments is generally observed in maraging steels due to the formation of intermetallic phases, and dramatic hardness increase [8,50,51]. However, the two alloys show higher Charpy impact toughness values in the over-aged condition (600 °C/3 h). The CVN data support the widely accepted fact that most engineering materials within a given microstructural class show higher toughness with a decrease in strength [52]. This is also in accordance with the work of Xavier et al. [53] where the effects of over-aging on the mechanical properties of a 18Ni300 maraging steel were studied, showing that softening accompanied by a certain amount of reverted austenite can be beneficial for the toughness of the material.

In general, the toughness of the Co–Ti free steels is lower than that of 18Ni300, due to the lower Ni contents. In the absence of Co, high Ni content impedes a fully martensitic microstructure, therefore its wt.% is normally reduced to tune the Martensite transformation temperatures. Moreover, it is reported that increase in Si + Mn content in maraging steels generally reduces notch toughness and impact energy [54,55]. Therefore, the most probable reason is the presence of higher amount of Si, and Mn in Co–Ti free material.

The current mechanical properties, especially in view of tensile strength and hardness, are in line with other Co free alternatives processed by PBF-LB. In a Co free, Ti (1 wt%) containing stainless maraging steel, Brytan et al. [56] reported a hardness of ~52 HRC, and a tensile strength of ~1600 MPa by ageing at 500 °C for 6 h. Another example is AM Corrax, a stainless Al (1.6 wt%) containing maraging steel, showing ~1600 MPa tensile strength, by 4 h of ageing at 525 °C, in both AM, and wrought condition [57]. In view of the absence of Ti, and minor additions of Al, the current alloy may offer improved polishability and cleanliness, while the two mentioned alternatives offer a much better corrosion resistance.

4. Concluding remarks

In this paper, the mechanical properties and the microstructural features of a novel Co–Ti free maraging steel, through the more cost-efficient IGA atomization route, for additive manufacturing were investigated. This alloy, which does not contain Co, Ti, and Al as alloying elements shows the potential to accelerate the transition to more sustainable and cost-effective production based on the following conclusions.

- The results confirmed the feasibility of achieving a nearly fully martensitic microstructure in as built (i.e., less than 3 vol% RA) and solution annealed (i.e., fully martensitic) conditions.
- After suitable aging, the novel alloy's maximum hardness, yield strength, and tensile strength were ~525 HV, 1475 MPa, and ~1600 MPa, respectively. The alloy has an elongation at break of 6.4% at this strength level, showing the possibility of obtaining ultrahigh strength levels with promising ductility.
- When compared to commercially available 18Ni300 maraging steels, DSC analysis revealed a delay in austenite reversion for the Co–Ti free alloy. Hardness curves confirmed lower softening kinetics at 525 °C. The improved softening resistance at elevated temperatures is promising in light of the novel alloy's applicability in tooling.
- Impact toughness showed a slight drop in Co–Ti free alloy compared with that of 18Ni300.
- With ultrahigh strength (~1600 MPa), and acceptable ductility (~6%), the Co, Ti, and Al free alloy has the potential to replace 18Ni300 in most of its intended uses.

Declaration of competing interest

The authors declare that they have no known competing financial interests or personal relationships that could have appeared to influence the work reported in this paper.

Appendix A. Supplementary data

Supplementary data to this article can be found online at https://doi.org/10.1016/j.jmrt.2024.03.088.

References

[1] da Fonseca DPM, Melo Feitosa AL, de Carvalho LG, Plaut RL, Padilha AF. A short review on ultra-high-strength maraging steels and future perspectives. Mater Res 2021;24:e20200470. https://doi.org/10.1590/1980-5373-MR-2020-0470.

[2] Vasudevan VK, Kim SJ, Wayman CM. Precipitation reactions and strengthening behavior in 18 Wt Pct nickel maraging steels. Metall Trans A 1990;21 A:2655–68. https://doi.org/10.1007/BF02646061/METRICS.

[3] Tewari R, Mazumder S, Batra IS, Dey GK, Banerjee S. Precipitation in 18 wt% Ni maraging steel of grade 350. Acta Mater 2000;48:1187–200. https://doi.org/10.1016/S1359-6454(99)00370-5.

[4] Rohit B, Muktinutalapati NR. Fatigue behavior of 18% Ni maraging steels: a review. J Mater Eng Perform 2021;30:2341–54. https://doi.org/10.1007/S11665-021-05583-W/FIGURES/12.

[5] Bajaj P, Hariharan A, Kini A, Kürnsteiner P, Raabe D, Jägle EA. Steels in additive manufacturing: a review of their microstructure and properties. Mater Sci Eng, A 2020;772:138633. https://doi.org/10.1016/J.MSEA.2019.138633.

[6] Tan C, Zhou K, Kuang M, Ma W, Kuang T. Microstructural characterization and properties of selective laser melted maraging steel with different build directions Microstructural characterization and properties of selective laser melted maraging steel with different build directions. Sci Technol Adv Mater 2018. https://doi.org/10.1080/14686996.2018.1527645.

[7] Casalino G, Campanelli SL, Contuzzi N, Ludovico AD. Experimental investigation and statistical optimisation of the selective laser melting process of a maraging steel. Opt Laser Technol 2015;65:151–8. https://doi.org/10.1016/J.OPTLASTEC.2014.07.021.

[8] Kempen K, Yasa E, Thijs L, Kruth JP, Van Humbeeck J. Microstructure and mechanical properties of selective laser melted 18Ni-300 steel. Phys Procedia 2011;12:255–63. https://doi.org/10.1016/J.PHPRO.2011.03.033.

[9] Kürnsteiner P, Wilms MB, Weisheit A, Barriobero-Vila P, Jägle EA, Raabe D. Massive nanoprecipitation in an Fe-19Ni-xAl maraging steel triggered by the intrinsic heat treatment during laser metal deposition. Acta Mater 2017;129:52–60. https://doi.org/10.1016/J.ACTAMAT.2017.02.069.

[10] Jägle EA, Sheng Z, Kürnsteiner P, Ocylok S, Weisheit A, Raabe D. Comparison of maraging steel micro- and nanostructure produced conventionally and by laser additive manufacturing. Materials 2017;10:8. https://doi.org/10.3390/MA10010008.

[11] Bai Y, Yang Y, Wang D, Zhang M. Influence mechanism of parameters process and mechanical properties evolution mechanism of maraging steel 300 by selective laser melting. Mater Sci Eng, A 2017;703:116–23. https://doi.org/10.1016/J.MSEA.2017.06.033.

[12] Mooney B, Kourousis KI, Raghavendra R. Plastic anisotropy of additively manufactured maraging steel: influence of the build orientation and heat treatments. Addit Manuf 2019;25:19–31. https://doi.org/10.1016/J.ADDMA.2018.10.032.

[13] Deirmina F, Davies PA, Casati R. Effects of powder atomization route and post-processing thermal treatments on the mechanical properties and fatigue resistance of additively manufactured 18Ni300 maraging steel. Adv Eng Mater 2022;24:2101011. https://doi.org/10.1002/adem.202101011.

[14] Ferreira DFS, Miranda G, Oliveira FJ, Oliveira JM, Pt M. Conventionally and SLM-manufactured 18Ni300 steel: mechanical and tribological behaviour in dry sliding against PP40 composite. Int. J. Adv. Manuf. Technol. 2022;(122):1245–58. https://doi.org/10.1007/s00170-022-09972-w.

[15] Król M, Snopiński P, Czech A. The phase transitions in selective laser-melted 18-NI (300-grade) maraging steel. J Therm Anal Calorim 2020;142:1011–8. https://doi.org/10.1007/S10973-020-09316-4/TABLES/3.

[16] Magnee A, Drapier JM, Coutsouradis D, Habraken L. cobalt-containing high-strength steels. 1974.

[17] Leyssens L, Vinck B, Van Der Straeten C, Wuyts F, Maes L. Cobalt toxicity in humans—a review of the potential sources and systemic health effects. Toxicology 2017;387:43–56. https://doi.org/10.1016/J.TOX.2017.05.015.

[18] Taxell P, Huuskonen P. Toxicity assessment and health hazard classification of stainless steels. Regul Toxicol Pharmacol 2022;133:105227. https://doi.org/10.1016/J.YRTPH.2022.105227.

[19] Li H, Liu Y, Liu B, Wei D. Synergistic enhancement of strength and ductility of cobalt-free maraging steel via nanometer-scaled microstructures. Mater Sci Eng, A 2022;842:143099. https://doi.org/10.1016/J.MSEA.2022.143099.

[20] Wei D, Li H, Liu Y, Zhao W, Liu B, Tominaga A, et al. Microstructure deformation mechanism of cobalt-free maraging steel: in-situ synchronous X-ray diffraction study. SSRN Electron J 2022. https://doi.org/10.2139/SSRN.4112845.

[21] Pawlak SJ. Comparative analysis of the properties of two maraging steels for advanced structural applications. Fastener: Rynek Elementów Złącznych 2022;nr 1.

[22] He YI, Yang KE, Sha W. Microstructure and mechanical properties of a 2000 MPa grade Co-free maraging steel n.d. .

[23] Fathy A, Mattar T, El-Faramawy H, Bleck W. Mechanical properties of new low-nickel cobalt-free maraging steels. Steel Res 2002;73:549–56. https://doi.org/10.1002/SRIN.200200027.

[24] Brytan Z, Król M, Benedyk M, Pakieła W, Tański T, Dagnaw MJ, et al. Microstructural and mechanical properties of novel Co-free maraging steel M789 prepared by additive manufacturing. Materials 2022;15:1734. https://doi.org/10.3390/MA15051734. 2022;15:1734.

[25] Deirmina F, Bettini E, Johnston MK, Casati R, Lupi G, Scanavini A, et al. Development of a Cobalt and Titanium free ultra-high strength maraging steel for laser powder bed fusion. In: Proceedings of advances in additive manufacturing with powder metallurgy; 2023.

[26] Andersson JO, Helander T, Höglund L, Shi P, Sundman B. Thermo-Calc & DICTRA, computational tools for materials science. Calphad 2002;26:273–312. https://doi.org/10.1016/S0364-5916(02)00037-8.

[27] https://thermocalc.com/solutions/solutions-by-application/additive-manufacturing/n.d..

[28] ASTM E92-82, Standard test methods for Vickers hardness and Knoop hardness of metallic materials. ASTM International n.d. .

[29] ASTM International. ASTM E23-23a, Standard test methods for notched bar impact testing of metallic materials n.d..

[30] Sha W, Cerezo A, Smith GDW. Phase chemistry and precipitation reactions in maraging steels: Part IV. Discussion and conclusions. Metall Trans A 1993;24:1251–6. https://doi.org/10.1007/BF02668193/METRICS.

[31] Albu M, Panzirsch B, Schröttner H, Mitsche S, Reichmann K, Poletti MC, et al. High-resolution microstructure characterization of additively manufactured x5crnicunb17-4 maraging steel during ex and in situ thermal treatment. Materials 2021;14:7784. https://doi.org/10.3390/MA14247784/S1.

[32] Bojack A, Zhao L, Morris PF, Sietsma J. In-situ determination of austenite and martensite formation in 13Cr6Ni2Mo supermartensitic stainless steel. Mater Char 2012;71:77–86. https://doi.org/10.1016/J.MATCHAR.2012.06.004.

[33] Deirmina F, Davies PA, Dixit N, Siriki R, Pellizzari M. Production and characterization of a modified hot work tool steel by laser powder bed fusion. Metall. Mater. Trans. A Phys. Metall. Mater. Sci. 2022;53:2642–51. https://doi.org/10.1007/S11661-022-06694-2/TABLES/5.

[34] Casati R, Lemke JN, Tuissi A, Vedani M. Aging behaviour and mechanical performance of 18-Ni 300 steel processed by selective laser melting. Metals 2016;6:218. https://doi.org/10.3390/MET6090218.

[35] Ungár T. Microstructural parameters from X-ray diffraction peak broadening. Scripta Mater 2004;51:777–81. https://doi.org/10.1016/J.SCRIPTAMAT.2004.05.007.

[36] Peters DT, Cupp CR. The kinetics of aging reactions in 18 per cent Ni maraging steels. AIME Met. Soc. Trans. 1966;236:1420–9.

[37] Nouri N, Li Q, Schneider R, Damon J, Schüßler P, Laube S, et al. Characterization of phase transformation and strengthening mechanisms in a novel maraging steel produced using laser-based powder bed fusion. Mater Char 2024;207:113522. https://doi.org/10.1016/J.MATCHAR.2023.113522.

[38] Menapace C, Lonardelli I, Molinari A. Phase transformation in a nanostructured M300 maraging steel obtained by SPS of mechanically alloyed powders. J Therm Anal Calorim 2010;101:815–21. https://doi.org/10.1007/S10973-010-0745-5/TABLES/4.

[39] Amirabdollahian S, Deirmina F, Harris L, Siriki R, Pellizzari M, Bosetti P, et al. Towards controlling intrinsic heat treatment of maraging steel during laser directed energy deposition. Scripta Mater 2021;201:113973. https://doi.org/10.1016/J.SCRIPTAMAT.2021.113973.

[40] Moshka O, Pinkas M, Brosh E, Ezersky V, Meshi L. Addressing the issue of precipitates in maraging steels – unambiguous answer. Mater Sci Eng, A 2015;638:232–9. https://doi.org/10.1016/J.MSEA.2015.04.067.

[41] Pardal JM, Tavares SSM, Terra VF, Da Silva MR, Dos Santos DR. Modeling of precipitation hardening during the aging and overaging of 18Ni–Co–Mo–Ti maraging 300 steel. J Alloys Compd 2005;393:109–13. https://doi.org/10.1016/J.JALLCOM.2004.09.049.

[42] Sha W, Cerezo A, Smith GDW. Phase chemistry and precipitation reactions in maraging steels" Part I . Introduction and Study of Co-Containing C-300. Steel 1993;24:1251–6.

[43] Sha W, Cerezo A, Smith GDW. Phase chemistry and precipitation reactions in maraging steels: Part II. Co-free T-300 steel. Metall Trans A 1993;24:1233–9. https://doi.org/10.1007/BF02668191/METRICS.

[44] Zhao K, Gao T, Yang H, Hu K, Liu G, Sun Q, et al. Enhanced grain refinement and mechanical properties of a high–strength Al–Zn–Mg–Cu–Zr alloy induced by TiC nano–particles. Mater Sci Eng, A 2021;806:140852. https://doi.org/10.1016/J.MSEA.2021.140852.

[45] Ma K, Wen H, Hu T, Topping TD, Isheim D, Seidman DN, et al. Mechanical behavior and strengthening mechanisms in ultrafine grain precipitation-strengthened aluminum alloy. Acta Mater 2014;62:141–55. https://doi.org/10.1016/J.ACTAMAT.2013.09.042.

[46] Magnee A, Drapier JM, Coutsouradis D, Habraken L, Dumont J. Cobalt-containing high-strength steels. A critical review of the physical metallurgy of cobalt-containing high-strength steels, and a survey of their processing, properties, and uses. 1974.

[47] Schnitzer R, Zinner S, Leitner H. Modeling of the yield strength of a stainless maraging steel. Scripta Mater 2010;62:286–9. https://doi.org/10.1016/J.SCRIPTAMAT.2009.11.020.

[48] Pereloma EV, Shekhter A, Miller MK, Ringer SP. Ageing behaviour of an Fe–20Ni–1.8Mn–1.6Ti–0.59Al (wt%) maraging alloy: clustering, precipitation and hardening. Acta Mater 2004;52:5589–602. https://doi.org/10.1016/j.actamat.2004.08.018.

[49] Li X, Yin Z. Reverted austenite during aging in 18Ni(350) maraging steel. Mater Lett 1995;24:239–42. https://doi.org/10.1016/0167-577X(95)00109-3.

[50] J-p K, Humbeeck VJ. Microstructure and mechanical properties of maraging steel 300 after selective laser melting n.d..

[51] Sha W, Ye A, Malinov S, Wilson EA. Microstructure and mechanical properties of low nickel maraging steel. Mater Sci Eng, A 2012;536:129–35. https://doi.org/10.1016/J.MSEA.2011.12.086.

[52] Kim BC, Park SW, Lee DG. Fracture toughness of the nano-particle reinforced epoxy composite. Compos Struct 2008;86:69–77. https://doi.org/10.1016/J.COMPSTRUCT.2008.03.005.

[53] Xavier V, Filho L, Ferreira Barros I, Ferreira Gomes De Abreu H. Influence of solution annealing on microstructure and mechanical properties of maraging 300 steel. Mater Res 2017;20:10–4. https://doi.org/10.1590/1980-5373-MR-2016-0257.

[54] Decker RF, Eash JT, Goldma n AJ. 18 pet Ni maraging steel. ASM Trans 1962;55(1. n.d.).

[55] Novak CJ, Diran LM. What are the effects of residual elements in maraging steels. JOM 1963;15:200–4. https://doi.org/10.1007/BF03378230.

[56] Brytan Z, Król M, Benedyk M, Pakieła W, Tański T, Dagnaw MJ, et al. Microstructural and mechanical properties of novel Co-free maraging steel M789 prepared by additive manufacturing. Materials 2022;15:1734. https://doi.org/10.3390/MA15051734.

[57] Wu MW, Ku SW, Yen HW, Ku MH, Chang SH, Ni K, et al. The synergic effects of heat treatment and building direction on the microstructure and anisotropic mechanical properties of laser powder bed fusion Corrax maraging stainless steel. Mater Sci Eng, A 2023;887:145744. https://doi.org/10.1016/J.MSEA.2023.145744.